Pergamon

Acta mater. 49 (2001) 4363–4374

Acta MATERIALIA

www.elsevier.com/locate/actamat

LENGTH SCALE AND TIME SCALE EFFECTS ON THE PLASTIC FLOW OF FCC METALS

M. F. HORSTEMEYER[1]†, M. I. BASKES[2] and S. J. PLIMPTON[3]

[1]Center for Materials and Engineering Sciences, Sandia National Laboratories, Livermore, CA 94551-0969, USA, [2]Los Alamos National Laboratory, MSG755, Los Alamos, NM 87545, USA and [3]Center for Computation, Computers and Math, Sandia National Laboratories, Albuquerque, NM 87185-1111, USA

(Received 27 December 2000; received in revised form 27 March 2001; accepted 27 March 2001)

Abstract—We examine size scale and strain rate effects on single-crystal face-centered cubic (fcc) metals. To study yield and work hardening, we perform simple shear molecular dynamics simulations using the embedded atom method (EAM) on single-crystal nickel ranging from 100 atoms to 100 million atoms and at strain rates ranging from 10^7 to 10^{12} s^{-1}. We compare our atomistic simulation results with experimental data obtained from interfacial force microscopy (IFM), nano-indentation, micro-indentation and small-scale torsion. The data are found to scale with a geometric length scale parameter defined by the ratio of volume to surface area of the samples. The atomistic simulations reveal that dislocations nucleating at free surfaces are critical to causing micro-yield and macro-yield in pristine material. The increase of flow stress at increasing strain rates results from phonon drag, and a simple model is developed to demonstrate this effect. Another important aspect of this study reveals that plasticity as reflected by the global averaged stress–strain behavior is characterized by four different length scales: (1) below 10^4 atoms, (2) between 10^4 and 10^6 atoms (2 μm), (3) between 2 μm and 300 μm, and (4) above 300 μm.

Keywords: Plastic flow; FCC metals

1. INTRODUCTION

Analysis of size scale effects and strain rate effects related to plasticity is studied in the context of molecular dynamics simulations. Few studies, if any, couple these size scale and strain rate effects in plasticity. At the macro scale, strain rate and temperature effects have been studied for many ductile metals [1–3]. Attention to plasticity at smaller size scales has included independent studies of indentation experiments, thin-wire torsion tests, and atomistic simulations. Experimental and some theoretical studies on size scale dependence related to plastic deformation followed after the seminal work of Hall [4] and Petch [5]. For example, recent studies such as those by Ma and Clarke [6], McElhaney *et al.* [7] and Michalske and Houston [8] examined grain size effects on yield and hardness for different face-centered cubic (fcc) metals. Nix and Gao [9] and Begley and Hutchinson [10] explained this plastic indentor size effect by modifying classical plasticity theory to include strain gradients, which are attributed to the presence of geometrically necessary dislocations. Thin-wire experiments like those of Fleck *et al.* [11] included wires with diameters down to 12 μm. In these experiments, a definite size scale effect was observed in torsion on the yield stress and plasticity of the wires. Fleck and Hutchinson [12, 13] later applied a strain-gradient theory to analyze the size scale effects they found. Daw and Baskes [14], Taylor and Dodson [15–17], Taylor [18], Holian and Lomdahl [19] and Hoagland and Baskes [20] have studied effects of dislocations on plastic response using atomistic methods. Kitamura *et al.* [21] examined nano-scale tensile bars of nickel employing molecular dynamics. The purpose of our study is to analyze spatial size scale and strain rate issues on yield and plasticity at the atomic scale, since little work has focused on this coupling.

The upper limit of atomic size is determined by the capability of the computing platform. When the model size is increased, more computational time is needed to attain a certain strain level. Otherwise, one can increase the strain rate to achieve that certain strain level, but then the applied strain rates must be large. This trade-off of model size and strain rate is illustrated schematically in Fig. 1. Here the time domain can be inversely related to the strain rate, so

† To whom all correspondence should be addressed. Fax: 001-510-294-3410.

E-mail address: mfhorst@sandia.gov (M. F. Horstemeyer)

1359-6454/01/$20.00
PII: S1359-6454(01)00149-5

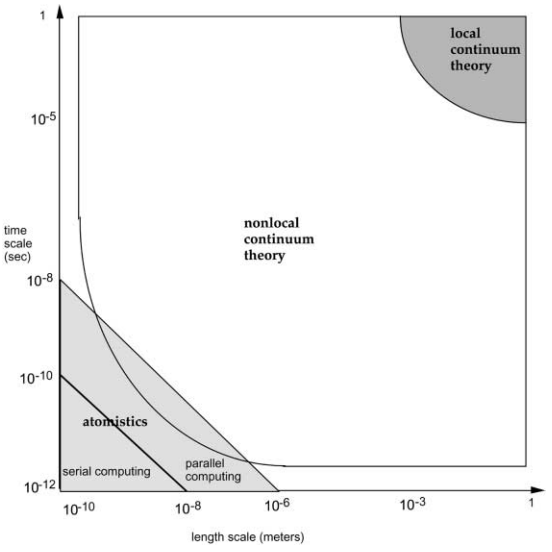

Fig. 1. Schematic illustration of strain rate and spatial size scale effects on computing and the regions where local and non-local continuum theories are applicable.

the time can be increased with decreasing strain rate and vice versa. If lower strain rates are desired, it is necessary to decrease the size of the atomic model because of the time needed to run the simulation. Our purpose in this paper is to broach the limits of current atomistic computing for examination of yield and plasticity of single-crystal nickel by using serial and parallel computing platforms. The schematic illustration in Fig. 1 indicates the regions where local and non-local continuum theories are applicable based on this study. Here, a non-local continuum theory is one in which a size scale is included within the structure of the governing equations.

2. ATOMISTIC BACKGROUND

We first start at the atomic scale by performing atomistic simulations at various length scales to analyze yield and plasticity. Daw and Baskes [14] proposed a numerical method for calculating atomic energetics, the embedded atom method (EAM). Daw *et al*. [22] reviewed the basic method and several applications of EAM. The major component of EAM is an embedding energy of an atom determined by the local electron density into which that atom is placed. A function, $\rho(r)$, is viewed as the contribution to the electron density at a site due to the neighboring atoms. The embedding energy F is associated with placing an atom in that electron environment. The functional form of the total energy is given by

$$E = \sum_i F^i\Big(\sum_{i\neq j}\rho^i(r^{ij})\Big) + \frac{1}{2}\sum_{ij}\phi^{ij}(r^{ij}), \tag{1}$$

where i refers to the atom in question and j refers to the neighboring atom, r^{ij} is the separation distance between atoms i and j, and ϕ^{ij} is the pair potential. Because each atom is counted, contravariant and covariant index notation is not used here. Subscripts denote the rank of the tensor; for example, one subscript denotes a vector, two subscripts denote a second-rank tensor, and so on. Superscripts identify the atom of interest. In molecular dynamics, the energy is used to determine the forces on each atom. At each atom the dipole force tensor, β (termed as the local stress tensor hereafter), is given by

$$\beta^i_{km} = \frac{1}{\Omega^i}\sum_{j(\neq i)}^{N} f^j_k r^{ij}_m, \tag{2}$$

where i refers to the atom in question and j refers to the neighboring atom, f_k is the force vector between atoms, r_m is a displacement vector between atoms i and j, N is the number of neighbor atoms, and Ω^i is the atomic volume. If stress could be defined at an atom, then β would be the stress tensor at that point. Since stress is defined at a continuum point, we determine the stress tensor (termed as the global continuum stress hereafter) as a volume average over the block of material,

$$\sigma_{mk} = \frac{1}{N}\sum_{i}^{N^*}\beta^i_{mk}, \tag{3}$$

in which the stress tensor is defined in terms of the total number of active atoms, N^*, in the block of material. We use this averaged stress to determine the stress–strain response and yield point of the block of material.

3. COMPUTATIONAL SET-UP

We perform classical molecular dynamics simulations using the following EAM potentials [14]: for nickel [23]; for copper [24]; and for aluminum [25, 26]. The EAM simulations were designed to mimic fixed-end, simple shear for different cross-sectional sample sizes and crystal orientations. As illustrated in Fig. 2(a), the computational block of material had free surfaces in the x- and y-directions with an aspect ratio of roughly 2:1 in x:y and was periodic in the $\underline{z}$-direction. The crystal orientation was [100, 011, 0$\bar{1}$1], and the shear loading on the y-face was in the [100] direction. We have chosen this orientation to investigate multiple slip. Our model has a quadruple slip orientation, with two equal primary slip planes with two equal directions for slip in each plane. For more details on the effects of crystal orientation, the reader is referred to Ref. [27]. The shear modulus for this nickel potential is 124.8 GPa. In previous work, Horstemeyer and Baskes [28] showed that in fixed-end

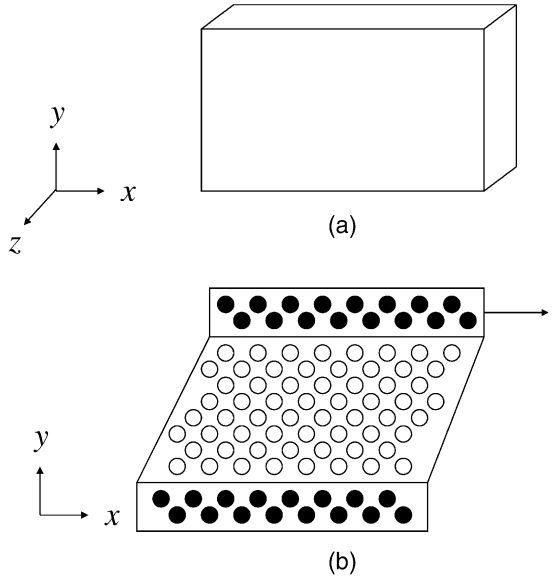

Fig. 2. Schematic illustration of simulation block of atoms at (a) the initial state and (b) at large strain in which the clear circles represent the active atoms and the dark circles represent the boundary atoms.

simulations the global continuum stress saturates if the *z*-direction is four or more unit cells in thickness; smaller samples introduce a separate size scale effect. Since one of our goals was to model as large a cross-sectional area as possible, we used a four-unit-cell *z*-direction thickness in our simulations.

After creating the samples with a desired crystal orientation, a few planes of atoms at the top and bottom (*xz*-planes at the $+y$ and $-y$ extrema) were frozen on their perfect lattice sites. The remainder of the atoms were allowed to relax to minimum energy to accommodate any surface relaxation at the two remaining free surfaces (*yz*-planes). Velocities of the interior (or active, non-frozen atoms) were then initialized using a Boltzmann distribution at a chosen temperature (300 K). For simple shear, a strain rate was then applied to the block of atoms by setting the *x*-velocity of the frozen *xz*-planes to a constant value. The bottom atomic plane had a prescribed *x*-velocity of zero for the duration of the dynamics simulation, and the top atomic plane had a prescribed constant velocity to create a strained sample as shown in Fig. 2(b).

If just the top row of atoms initially experienced the prescribed velocity without the active internal atoms experiencing the same velocity field, a shock would be induced into the block of material because of the high strain rates. In our calculations, we introduced an initial velocity field that mitigated the shock wave and then applied the boundary velocity fields. To accomplish this, the interior atoms in the model were also given an initial *x*-velocity (superposed on their thermal 300 K velocities) that varied linearly from 0.0 to the prescribed velocity at the top atomic plane depending on their *y*-coordinates in the simulation box. In these simulations, the prescribed velocity was chosen to model strain rates ranging from 10^7 s^{-1} to 10^{12} s^{-1}.

Following initialization, a constant number of atoms, constant volume and constant temperature (NVT) simulation was performed with a 0.001 ps time step until the block of atoms had undergone strain sufficient to create yield, typically a few per cent strain or more. Because straining via moving the frozen planes adds considerable energy to the active atoms, a Nose–Hoover thermostat [29, 30] was used during the molecular dynamics simulation to keep the active atoms at constant temperature. The thermostat applies a damping (or acceleration) factor to the active atoms based on the difference between their current temperature and the desired temperature (300 K). We computed the instantaneous temperature of the ensemble of active atoms after first subtracting from each atom the non-thermal *x*-velocity that was initially prescribed, since the active atoms essentially maintain the same component of *x*-velocity for the simulation.

Because this study focused on plasticity, the notion of a yield is important. In this context, we define two micro-yield points and a macro-yield point. First, the average global stress of the active atoms was computed by using equation (3), and a stress–strain curve was generated. Figure 3 shows stress–strain curves for atomistic simulations of 10,000 and 10 million atoms just to illustrate the behavior at different material block sizes. We identify three locations on the curve. The first location is defined as micro-yield 1, where the stress–strain behavior first deviates from elastic linearity, i.e., the proportional limit. At this point, initial dislocations are emitted from the surface because of the local stress gradients in the corners due to the boundary conditions. The second location is micro-yield 2, which is defined by the macro-scale continuum concept of a 0.2% offset strain. The third location is defined as macro-yield, the point at which the maximum stress occurs. We also define the quantity $\Delta\varepsilon_{\text{yield}}$, which is the difference in strain between the macro-yield and micro-yield 2. Because we start with a perfect lattice, there are no initial defects. As such the stress–strain responses, in terms of the stress drop-off, look very similar to experimental data of metal "whiskers" that have essentially no initial defects (cf. [31]). In whiskers, yield is typically defined at the "macro-yield" point. At this point, the stress required to activate a certain density of dislocations is reached and the material plastically deforms, precipitating dislocations with subsequent propagation of local Luders bands that lead to irregular fluctuations in the plateau region of the stress–strain curve after the macro-yield stress drop-off. These two curves illustrate that micro-yield 1 and micro-yield 2 are essentially the same and in many cases, as exemplified in the 10,000-atom simulation, macro-yield is very close to the other two micro-yield points.

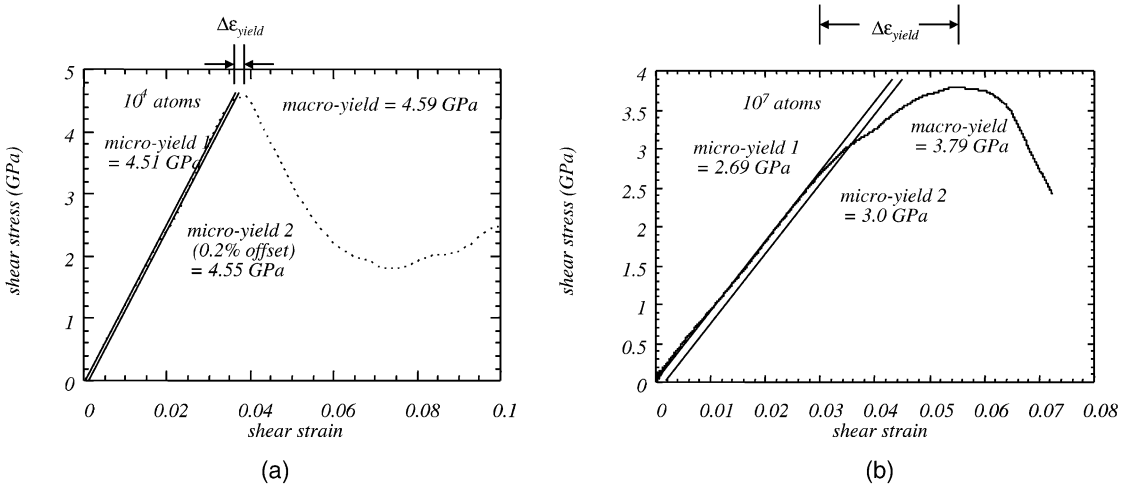

Fig. 3. Shear stress–strain curve of material blocks at an applied strain rate of $2.4\times10^{8}\ s^{-1}$ with (a) 10,000 atoms and (b) 10 million atoms, showing micro-yield 1 at the proportional limit, micro-yield 2 at 0.2% offset strain, and macro-yield.

In determining the yield points in many of the simulations, we also unloaded the material block at each of the micro-yield and macro-yield points to give information regarding permanent set and the influence of dislocations on the yield points. In Fig. 4, we show the atom positions at different locations along a simple shear deformation path for a block of nickel with 2242 atoms. Here, we unloaded at micro-yield 1 and micro-yield 2.

The type of simulation shown in Fig. 4 was typical of the ones that we performed with differing block sizes of material that ranged from 100 atoms to 100 million atoms, and the time steps from a few thousand to many millions depending on the applied strain rate. The largest simulations were run using a parallel version of the EAM code designed for distributed memory supercomputers (cf. [32]). Consequently, the CPU cost of the simulations also varied from a few seconds

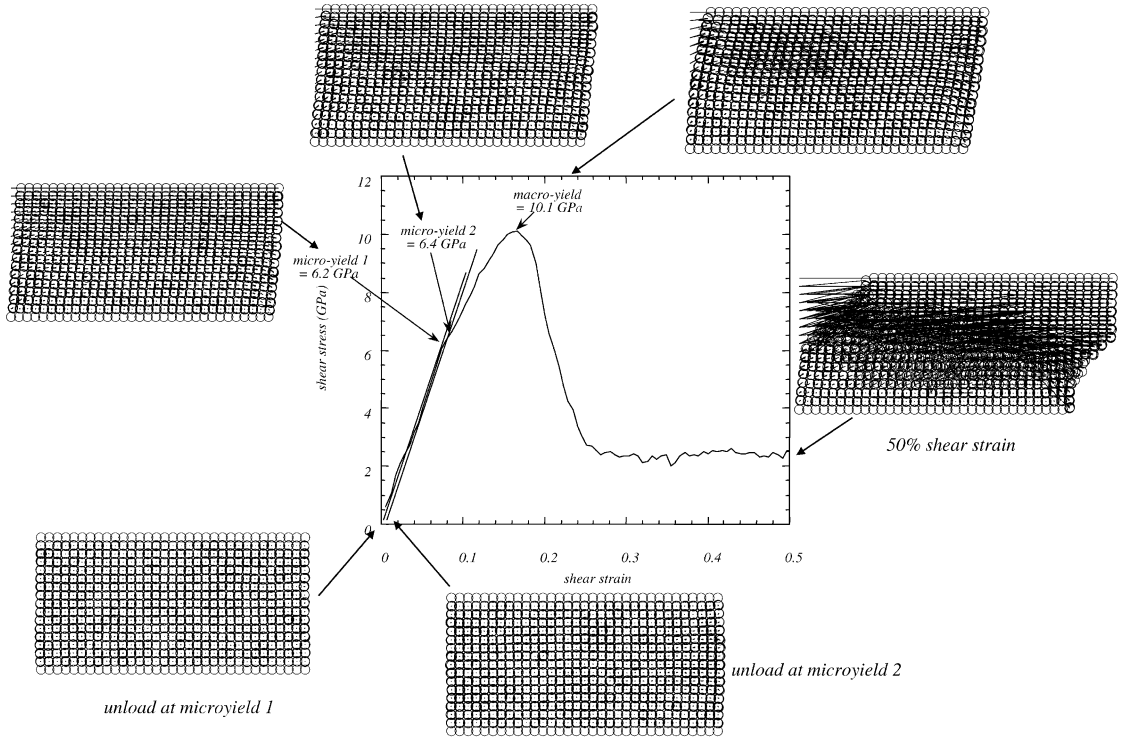

Fig. 4. Shear stress–strain curve for 2242 atoms of nickel illustrating atomic positions and relative displacements (denoted by arrows on atoms) at different strain levels.

on a single processor workstation to many hours on hundreds of processors on the Sandia/Intel Teraflop machine. In fact, the largest simulation took 13 CPU hours on 3000 processors.

4. ATOMISTIC RESULTS

There are two main themes we would like to discuss separately regarding the results, which are the effects of size scale and time scale. Unfortunately, they are linked together, so discussing one of these topics independently is difficult without begging questions about the other. However, we shall try to do so by first starting with time scale issues as related to strain rate effects on dislocation nucleation, motion and interaction. Recall from Fig. 1 that a competition between the size scale and time scale in performing atomistic simulations exists. If a strain rate of 10^7 s^{-1} is to be achieved in the current molecular dynamics paradigm, one must have a small number of atoms. The converse is also true. If a large block of atoms is desired, the applied strain rate must be rather high ($\sim 10^9$ s^{-1}). The reason for this time–space relation in the computations is related to the time scale of the atomic period involved, and this in turn affects the applied strain rates. With this in mind, we briefly address the time domains pertinent to our simulations.

4.1. Strain rate effects

There are several time domains to consider when considering strain rate effects on small specimens. First, the highest-frequency component will arise in relation to the atomic frequency. These vibrations occur on the order of 10^{-12} s. If shock is involved, then the longitudinal elastic shock wave velocity can be derived from the wave equation given by

$$C_{\text{elastic}} = \sqrt{\frac{K + 4/3G}{\rho}}, \tag{4}$$

and the plastic wave speed as

$$C_{\text{plastic}} = \sqrt{\frac{K}{\rho}}, \tag{5}$$

and the shear (or distortional) wave speed as

$$C_{\text{shear}} = \sqrt{\frac{G}{\rho}}, \tag{6}$$

in which ρ is the density of nickel, K is the bulk modulus and G is the shear modulus. Typical sound speeds are ~20 Å/ps. Since our blocks of material are small, shock waves propagate through the material many times on the time scale of our simulations which achieve large strains (~30%). However, in our simulations, we avoid the shock by initializing all the atoms with an initial velocity gradient in the x-direction as discussed above, thus alleviating the time issue with the shock wave.

Another time domain to consider is that of the dislocation motion. Baskes and Daw [33] showed that the modified Leibfried [34] continuum equation for dislocation velocity can be used to explain the atomistic simulations in simple shear for nickel:

$$\frac{\mathrm{d}}{\mathrm{d}t}\frac{mv}{\sqrt{1-(v/c)^2}} = (\sigma-\sigma_0)b - a\frac{3\mathrm{k}T}{10b^2}\frac{v/c}{\sqrt{1-(v/c)^2}}, \tag{7}$$

where m is the dislocation per unit mass length (0.2 atoms/Burger's distance), c is the dislocation terminal velocity or sound speed (20 Å/ps), σ is the applied stress, σ_0 is the friction stress (4 MPa), b is the Burger's vector of the dislocation (2.5 Å for nickel), and α is a dimensionless drag constant (0.98). The above values for nickel were determined in Ref. [33]. A closed-form solution can then be used to track the dislocation motion. The left-hand side is the time rate of change of the dislocation momentum. The first term on the right-hand side is the driving force for motion, and the second term is the dissipation due to dislocation–phonon drag, which is the important factor related to the applied strain rate. Baskes and Daw [33] added the relativistic factor in the drag term to allow an analytical solution of the equation. Consider a dislocation nucleated a distance x_0 from a free surface. We modify equation (7) to include image forces due to the nature of the free surfaces in the present atomistic simulations and to remove the relativistic factor in the drag term:

$$\frac{\mathrm{d}}{\mathrm{d}t}\frac{mv}{\sqrt{1-(v/c)^2}} = \sigma_{\text{eff}}b - a\frac{3\mathrm{k}T}{10b^2}(v/c), \tag{8}$$

in which σ_{eff} is defined as

$$\sigma_{\text{eff}} = \begin{cases} 0 & \sigma \le \sigma_{\text{I}} + \sigma_0/M \\ M(\sigma-\sigma_{\text{I}})-\sigma_0 & \sigma > \sigma_{\text{I}} + \sigma_0/M \end{cases} \tag{9}$$

σ_{I} is the stress due to image forces and is related to the nucleation stress, σ^*, as follows:

$$\sigma_{\text{I}} = \frac{x_0}{x}\sigma^*, \tag{10}$$

where x is the current dislocation position, and M is the orientation factor related to the resolved shear stress. Here, we assume that the dislocation is nucleated at time zero at position x_0 from the surface when the applied shear stress equals the nucleation

stress. The dislocation accelerates under increasing load. When a 0.2% plastic strain offset is assumed for yield, the only free parameter in the model is the nucleation stress σ^*, which is chosen to agree with the atomistic simulations. The nucleation stress is the only size-dependent quantity in the model.

The next time domain of importance is related to the applied strain rate. In our simulations, we start with a strain rate on the order of the atomic period (10^{12} s^{-1}) and then decrease it five orders of magnitude (10^7 s^{-1}). A critical peak strain rate exists in which the stress is so high that the lattice strength of the crystal is reached and immediate fracture occurs between the atoms with the applied boundary condition and the adjacent atoms. The results that we show do not include these data, since we are not concerned with fracture in our study. When the applied strain rate is between the peak fracture strain rate and the time domain in which dislocation inertial effects are important, the global yield stress increases with increasing model size. When the applied strain rate is below this regime, then the yield stress increases with decreasing spatial size. In any event, as the applied strain rate increases, the yield stress and the magnitude of the stress drop increase as expected from phonon drag.

Given this information, we ran several atomistic simulations at different sizes and applied strain rates and determined the yield stresses based on a 0.2% strain offset. The stress–strain curves are presented in Figs 5–11 for different atomistic model sizes. These figures show that as the strain rate increases, the flow stress increases. The yield stresses, normalized by the shear modulus, for the different nickel simulations are shown in Fig. 12. The strain rate behavior as discussed above is only observed for the intermediate size samples. For these samples we see that at relatively small strain rates, the yield stress is independent of strain rate, while at higher strain rates the

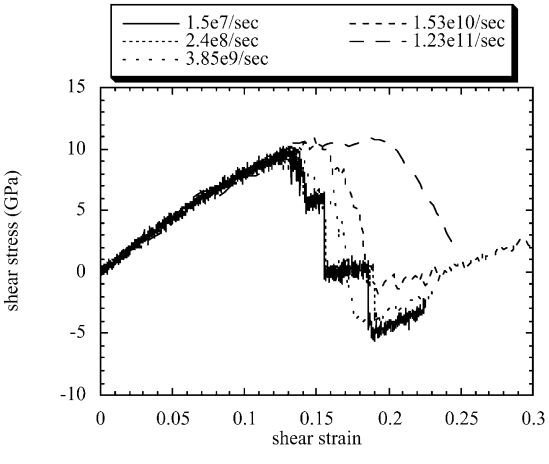

Fig. 5. Shear stress–shear strain curves of material block with 196 atoms (length is 2.8 nm and height is 1.4 nm) at strain rates from 1.5×10^7 s^{-1} to 1.23×10^{11} s^{-1}, illustrating the increase in yield as a function of strain rate.

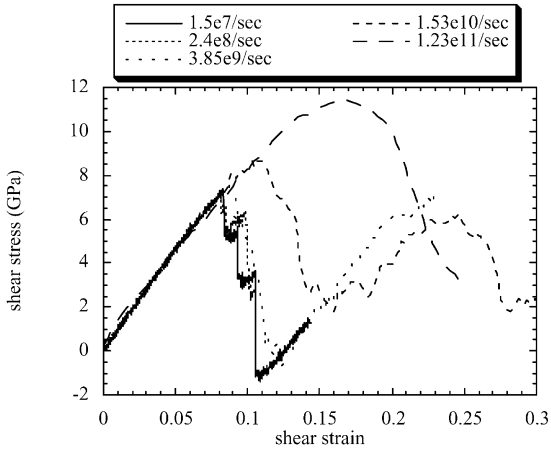

Fig. 6. Shear stress–shear strain curves of material block with 1384 atoms (length is 7.8 nm and height is 4.0 nm) at strain rates from 1.5×10^7 s^{-1} to 1.23×10^{11} s^{-1}, illustrating the increase in yield as a function of strain rate.

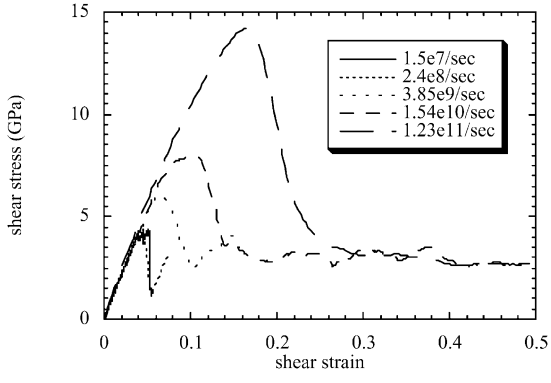

Fig. 7. Shear stress–shear strain curves of material block with 2×10^4 atoms (length is 0.0282 μm and height is 0.014 μm) at strain rates from 1.5×10^7 s^{-1} to 1.23×10^{11} s^{-1}, illustrating the increase in yield as a function of strain rate.

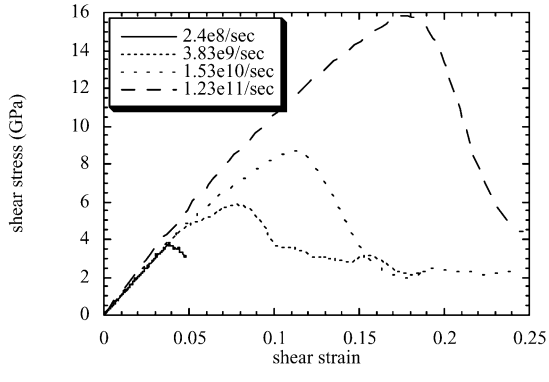

Fig. 8. Shear stress–shear strain curves of material block with 1×10^5 atoms (length is 0.057 μm and height is 0.021 μm) at strain rates from 1.5×10^7 s^{-1} to 1.23×10^{11} s^{-1}, illustrating the increase in yield as a function of strain rate.

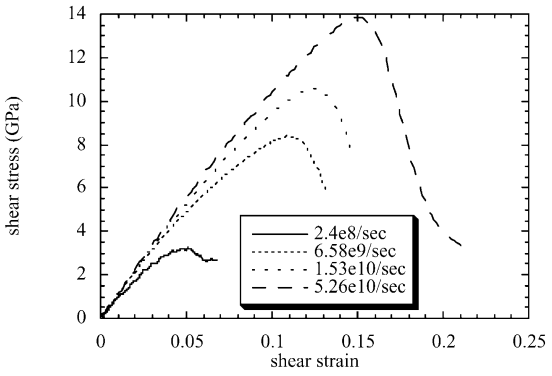

Fig. 9. Shear stress–shear strain curves of material block with 1×10^6 atoms (length is 0.18 μm and height is 0.07 μm) at strain rates from 1.5×10^7 s^{-1} to 1.23×10^{11} s^{-1}, illustrating the increase in yield as a function of strain rate.

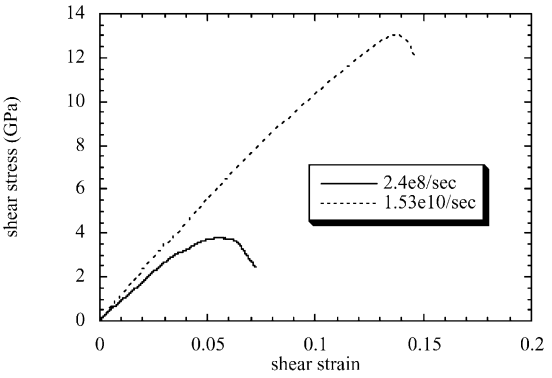

Fig. 10. Shear stress–shear strain curves of material block with 1×10^7 atoms (length is 0.55 μm and height is 0.21 μm) at strain rates from 1.5×10^7 s^{-1} to 1.23×10^{11} s^{-1}, illustrating the increase in yield as a function of strain rate.

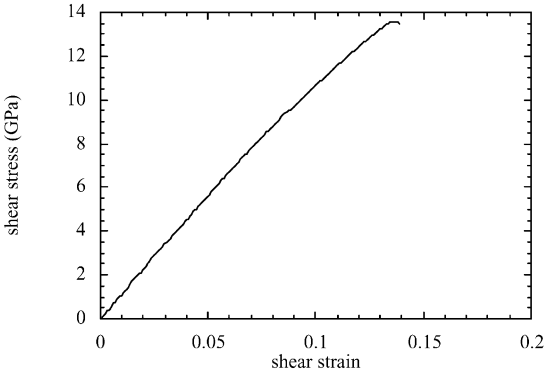

Fig. 11. Shear stress–shear strain curves of material block with 1×10^8 atoms (length is 1.7 μm and height is 0.7 μm) at a strain rate of 1.53×10^{10} s^{-1}.

yield stress increases rapidly. For the small samples the extreme increase in yield stress is subsumed by the fracture regime (not shown). For the large samples, due to computer limitations, we were not able to calculate strain rates low enough to reach the strain-rate-independent regime.

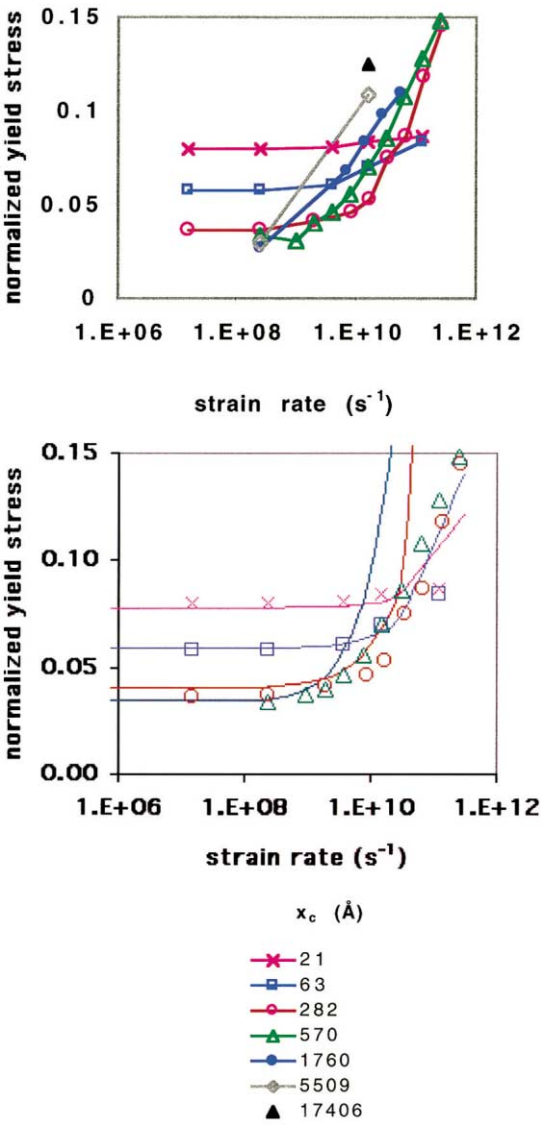

Fig. 12. Yield stress normalized by the shear modulus as a function of strain rate, comparing atomistic simulations (dots) and the dislocation model (solid line). Various curves represent different model sizes.

In Fig. 12 we also compare the same atomistic data to the simple model presented above. The choice of the nucleation stress as a function of size is discussed below. We see that the simple model captures the qualitative features of the data: strain rate independence at low strain rate; a rapid increase in yield stress at a critical strain rate; and an increase in the critical strain rate with decreasing sample size. We designate the stress level in the strain-rate-independent region (low strain rate) as a plateau stress. The decrease in this plateau stress with increasing sample size is not a prediction of the model, but was input as the size dependence of the dislocation nucleation stress. However, the existence of the strain-rate-independent region is a direct consequence of the model. The dislocation model predicts an

increase in yield stress at high strain rates more rapid than the atomistic simulations. This effect is due to the fact that we have only allowed the nucleation of one dislocation, that is, the dislocation density is constant. At the higher strain rates, multiple dislocations are nucleated, lowering the yield stress from the model calculation prediction. For comparison, Fig. 13 shows experimental curves for single-crystal copper illustrating that the trend for increasing flow stress with increasing applied strain rate occurs for other metals as well. All of the strain rate features noted above for the simulations and the dislocation model have also seen in the experimental data (cf. [35, 36]). Note that the critical strain rate in the calculations is significantly higher than that of the experiments. This behavior is expected from the model since the size scale for the experiments is significantly larger than for the calculations. Also note that stress scale for the experiments is significantly lower than for the calculations. Again this behavior is consistent with the model, since the plateau stress (rate-independent) is size-dependent. We will return to the size dependence in the next sub-section.

Again referring to Figs 5–11, we see that the micro-yield and macro-yield both increase with increasing applied strain rate. However, an increase in applied strain rate increases the strain difference ($\Delta\varepsilon_{\text{yield}}$) between the micro-yield and macro-yield. This effect also occurs as the model size increases as shown in Fig. 3. For the high applied strain rate, the reason that the strain difference increases between the micro-yield and macro-yield point is due to the time domains in which the dislocation nucleation rate and velocity are of different magnitudes than the applied strain rate. As such, at low dislocation densities and at low dislocation velocities, the applied strain cannot be fully accommodated by dislocation propagation, so a lower modulus arises that looks like work hardening between the micro-yield and macro-yield. The larger size blocks of atoms exacerbate this effect.

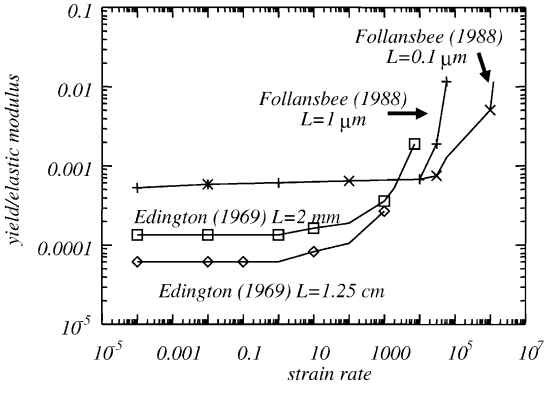

Fig. 13. Experimental data examining yield stress versus applied strain rate from Follansbee [36] and Edington [35] for copper.

4.2. Size scale effects

When the nickel data in Figs 5–11 are rearranged according to spatial size, we can see that a size scale effect arises as shown by the stress–strain curves in Fig. 14 at a strain rate of 2.4×10^{8} s^{-1}. This size scale effect is also observed in copper as shown in Fig. 15 at a strain rate of 10^{9} s^{-1}. In a companion paper [37], we examine different size scale effects on single-crystal copper in simple shear and torsion.

We may also compare the plateau yield stresses as a function of specimen size. In Fig. 16 we show the normalized yield stress as a function of the *x*-dimension size of the model. Note that the models considered here have the *z*-dimension constant and the *x*:*y* aspect ratio fixed at ~2:1, so that the single *x*-dimension fully characterizes the model. We see a clear power-law dependence of the plateau (rate-independent) yield stress, with the stress varying as model size to the $-1/4$ power. This dependence was used to define the size dependence of the dislocation nucleation stress σ^{*} in the dislocation model calculations presented above in Fig. 12.

In our simulations, the dislocations nucleate at the free surfaces. These free surfaces can be thought of as true free surfaces or a grain boundary. In either case, it is energetically favorable to generate dislocations in the corners of the specimen because of equilibrium considerations with the applied shearing. In pure shear a balance in applied boundary conditions exists, but in our simple shear simulations this does not exist. As a result a continuum spin which resolves into elastic and plastic components arises. It is this rotational component that affects the dislocation nucleation. A more detailed explanation can be found in Ref. [27].

5. SIZE SCALE EFFECTS AND VARIOUS EXPERIMENTS

Figures 14 and 15 show size scale effects in the stress–strain response for single-crystal nickel and copper. The goal here was to illustrate that another fcc metal, besides nickel, experiences a similar size scale effect in terms of increasing size decreasing the yield stress. If this size scale effect is universal, what is an appropriate length scale parameter?

In trying to understand yield at different length scales, we need to have a common length scale parameter. For this purpose, we choose volume to surface area as our metric. This volume to surface area can be defined very clearly for each test method and atomistic simulation. Table 1 summarizes the values for the analysis performed in this study related to the specimen geometries.

Figure 17 shows a log–log plot of yield stress under simple shear (atomistics) and torsion and indentation (experiment) normalized by elastic shear modulus and resolved on a (111) slip plane as a function of the characteristic length scale given by the volume-to-

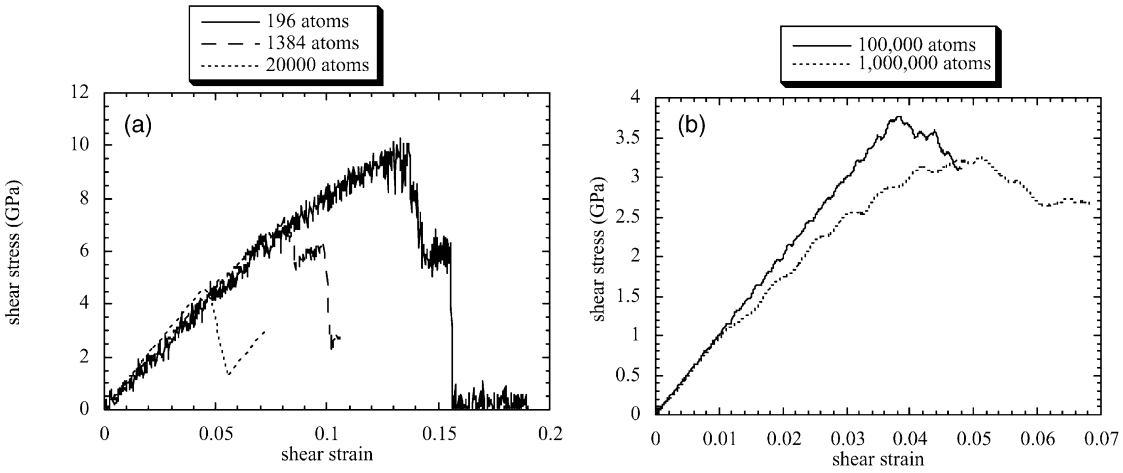

Fig. 14. Shear stress–strain curves of various size atomistic models at an applied strain rate of 2.4×10^{8} s^{-1} for (a) 196 atoms, 1384 atoms and 2×10^{4} atoms and (b) 10^{5} atoms, 10^{6} atoms and 10^{7} atoms.

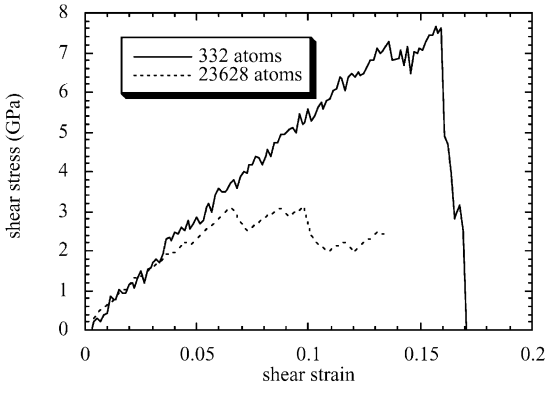

Fig. 15. Shear stress–strain curve of two atomistic models showing the differences in yield and work hardening for single-crystal copper at a strain rate of 10^{9} s^{-1}.

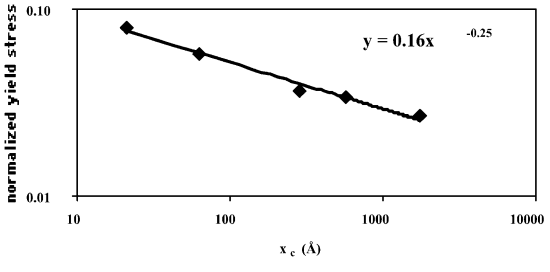

Fig. 16. Rate independent yield stress normalized by the shear modulus as a function of the size (*x*-dimension) of the atomistic model. The equation for the power-law behavior is shown.

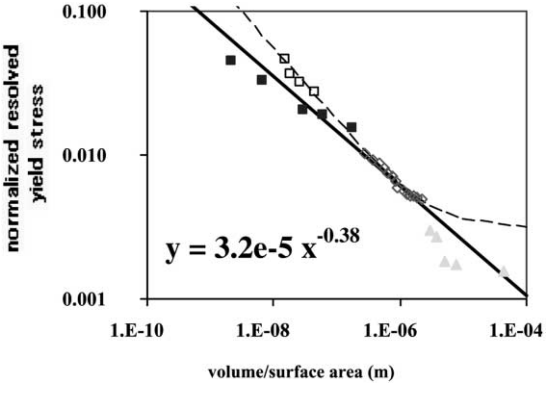

Fig. 17. Yield stress normalized by the elastic modulus and resolved on a (111) slip plane versus volume to surface area for nickel, gold and copper for various experiments and atomistic simulations: ■, EAM (present work); □, Michalske and Houston [8]; ◇, McElhaney *et al.* [7]; ▲, Fleck *et al.* [11]; – – –, Nix and Gao [9]; ———, power law. The equation for power-law behavior is shown.

surface-area ratio. This plot shows a clear size scale effect. The atomistic results come from the current molecular dynamics calculations in the plateau (rate-independent) region of (low) strain rate. A factor of 0.577 for the resolved shear stress was applied to the data of Fig. 16.

The experimental torsion data (Fleck *et al.* [11]) shown in Fig. 17 are from small-scale torsion tests of polycrystalline copper at a strain rate of 10^{-3} s^{-1} at room temperature. The volume to surface area was

Table 1. Volume to surface areas for various geometries

Geometry	Volume	Surface area	Volume to surface area
Simple shear (cell dimensions: x_c, y_c, z_c)	$x_c y_c z_c$	$2y_c z_c$	$x_c/2$
Torsion (cylinder radius: r, height: h)	$\pi r^2 h$	$2\pi rh$	$r/2$
IFM (contact radius: a)	$2/3\pi a^3$	πa^2	$2/3a$
Indentation (contact radius: a, indentation depth: h, indentor tip angle: θ)	$2/3\pi a^3$	πa^2	$2/3a = 2/3\times h/\tan\theta$

chosen to be the torsion specimen radius divided by two (Table 1). To obtain the maximum shear stress at the surface of the cylinder, the normalized torque data presented in the manuscript were multiplied by $\pi/3$ and divided by the shear modulus of copper. It was assumed that at least one grain in the polycrystalline sample was oriented perfectly for slip, hence no resolution factor was applied. This analysis gives an upper bound on the resolved yield stress.

Indentation hardness, H, of ductile metals is considered a measure of the yield stress in compression, $H = 3\times$yield [38]. Although inadequate measurement techniques and surface contaminants can cause apparent increases in hardness at small loads, the bulk of the data from many experimenters illustrates a common thread of increased hardness, and subsequently yield, as the size scale decreases. McElhaney *et al.* [7] illustrated the size dependence on yield for both single-crystal and polycrystalline copper. McElhaney *et al.*'s single-crystal data [7] are included in Fig. 17. To determine the appropriate length scale, we consider the size of the volume of copper under the indentor that has plastically deformed. A reasonable assumption is to take that volume as a hemisphere with radius equal to the contact radius [9]. The surface area is taken as the contact area. A resolution factor of 0.228 [39] and tip angle of $\tan\theta = 0.358$ were used.

Interfacial force microscopy (IFM) data for gold from Michalske and Houston [8], which are also plotted on Fig. 17, appear to align very nicely, albeit a bit higher, with the atomistic results. The difference may be due to the fact that the atomistic data are rate-independent values and a higher, changing strain rate occurs in the IFM data. Here, the total volume to surface area was determined for the spherical indentor as 2/3 of the contact radius (see Table 1), which is determined by simple geometry from the tip radius and the indentor depth at yield. The yield stress was calculated using the Hertz model and the shear stress data presented in the experimental manuscript. A resolution factor of 0.228 [39] was applied to the applied stress. Michalske and Houston's [8] argument that dislocation nucleation governs yield stress at this length scale compares extremely well with the work of Horstemeyer and Baskes [28].

We have also examined nanocrystalline metals in the context of the volume to surface area but found much scatter in the data and as such the data are not plotted here. Masumura *et al.* [40] have reviewed many studies on nanocrystalline materials and concluded that the Hall–Petch relation operates above a certain length scale, but not below that particular level. Their data indicate that that the Hall–Petch relation does not work in tension. As mentioned earlier, by analyzing the length scale effect in tension other competing dissipative mechanisms can contribute to the stress–strain or hardness behavior, in particular void nucleation or growth. With these different mechanisms involved we deemed it unfruitful to include these data.

One last comment regarding the size scale effect is warranted. In Fig. 17 are the results of a simple model using the concept of geometrically necessary dislocations by Nix and Gao [9]. The model was fit to the McElhaney *et al.*'s [7] single-crystal data. We see that extrapolation of this model to smaller length scales yields good agreement with the Michalske and Houston [8] data and fair agreement with the atomistic simulations. Note that the model does not agree at all with the torsion data. In contrast, a simple power law seems to represent all of the data reasonably well in which the only argument needed is that related to dislocation nucleation.

6. SIZE SCALE PLASTICITY DOMAINS

By examining the global stress–strain responses of the atomistic simulations, we observed two forms of bulk plastic behavior depending on the size of blocks of atoms. Coupling this computational information with experimental data from others (cf. [11]), we assert that four regions of bulk plastic behavior exist based upon the size scale of the solid medium, as summarized schematically in Fig. 18. The first spatial domain is roughly below about 10,000 atoms, less than 200 Å. The exact size varies depending upon the crystal orientation, strain rate, temperature and boundary conditions, but it is approximately this scale. Here, the local atomic vibrations play a critical role, and three characteristics of the stress–strain curve are demonstrated: high-frequency stress oscillations throughout the stress–strain curve and a stress drop-off after macro-yield. To employ a continuum plasticity model in this spatial domain, a vibration analogy with a size scale parameter would be appropriate (cf. [28]). In terms of computations, these simulations were performed in a serial environment.

Above several thousand atoms and below 100 million atoms (about 2 μm), the high-frequency stress oscillations are dampened out because of the averag-

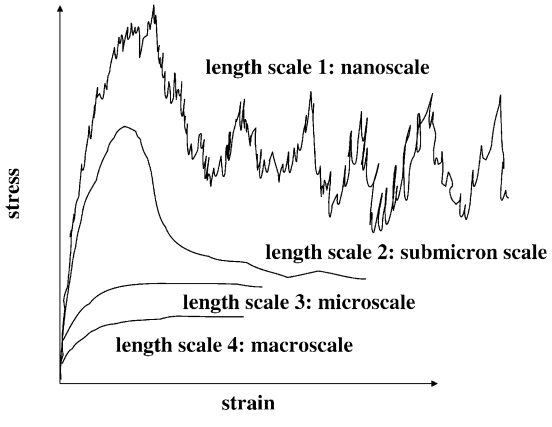

Fig. 18. Schematic showing the stress–strain responses at four different size scales.

ing procedure used to determine the global continuum stress. However, the post-yield stress drop-off occurs. We note here that a stress drop-off is observed in indentation and IFM experiments after dislocation nucleation [41]. To model this spatial domain with a continuum plasticity model, a theory that includes a size scale is needed. In terms of computations, these simulations were performed in a parallel environment.

For single-crystal, nearly dislocation-free material, these two smaller regions are dominated by dislocation nucleation and not by the morphological distribution or number density of dislocations. As discussed earlier, the stress–strain response looks much like that of a whisker in this region. Figure 18 shows a comparison of stress–strain responses for two different sizes illustrating the two different plasticity regions. Note that, as the size increases, the yield stress decreases. We discuss these trends with relatively small blocks of atoms elsewhere [28].

In the third spatial domain between 2 μm (approximately) and 300 μm, the stress drop-off does not exist and micro-yield and macro-yield start to converge, but a length scale dependence is still obtained as evidenced in Fleck *et al*. [11]. Since our arguments are based upon single-crystal information, future single-crystal experiments are planned. However, we expect a similar size scale response as observed in Fleck *et al*.'s [11] data. Above 300 μm, a power-law function without a size scale parameter can describe the stress–strain response. Although single-crystal whiskers can be obtained in spatial domains 2 and 3, the Fleck *et al*. [11] data relate to polycrystalline metals. For the polycrystals, dislocation nucleation is not as dominant as the dislocation number density and morphological distribution in determining the stress state. Hence, there is a gradual change of influence from dislocation nucleation at much smaller scales to dislocation number density and distribution at larger scales. Fleck *et al*. [11] conducted torsion tests of polycrystalline copper that ranged from 12 μm to about 300 μm. Their data revealed that a stress drop-off did not exist after macro-yield but a length scale effect did indeed exist when determining yield and the work-hardening rate. The length scale effect seems to disappear at about 300 μm, thus defining the demarcation between the third and fourth spatial domains of plasticity. The main difference between the third and fourth domains is essentially a size scale dependence in the third domain and no size scale dependence in the fourth.

In this fourth spatial domain, no oscillations, stress drop-offs or size scale dependence is found based on experimental observations. In this domain atomistic simulations are currently out of reach for even parallel computing. However, as computers get faster, atomistic simulations will be able to be performed in this region in the near future. As far as continuum modeling, local continuum models have been used to solve engineering problems in this spatial domain fairly well.

7. CONCLUSIONS

Atomistic simulations using the embedded atom method have been performed for nickel samples containing 100 to 100 million atoms. Using molecular dynamics the samples were deformed in simple shear at 300 K at strain rates ranging from 10^7 to 10^{12} s^{-1}. It was found that samples with less than ~1000 atoms showed little dependence of the yield stress on strain rate. Larger samples showed significant increases in yield stress with increasing strain rate. At the lower strain rates the yield stress approached a constant value which depended on sample size. The transition strain rate where the yield stress became independent of strain rate decreased with increasing sample size. The simulations showed that the yield phenomenon was directly related to dislocation nucleation at free surfaces. Using this concept, a simple inertial dislocation model has been developed that captures these features.

A size scale, based on the volume to surface area of the sample, has been postulated. Using this scaling concept, the yield stress of the atomistic simulations was compared with experimental measurements using indentation and torsion techniques. A simple power-law scaling was found. It is noteworthy that the size scale effect is shown for simple shear, a stress state in which there are no strain gradients. In light of these results, it is suggested that dislocation nucleation, rather than the concepts of geometrically necessary dislocations or strain-gradient plasticity, should be considered as an explanation of plasticity size effects.

Acknowledgements—This work was performed under the US Department of Energy contract numbers DE-AC04-94AL85000 and W-7405-ENG-36. Discussions with Doug Bammann were enlightening regarding the role of dislocations on the stress state.

REFERENCES

1. Johnson, G. R. and Holmquist, T. J., in *Report LA-11463-MS*. Los Alamos National Laboratory, Los Alamos, NM, 1988.
2. Bammann, D. J., Chiesa, M. L., Horstemeyer, M. F. and Weingarten, L. I., in *Structural Crashworthiness and Failure*, ed. N. Jones and T. Weirzbicki. 1993, p. 1.
3. Gray, G. T., Chen, S. R., Wright, W. and Lopez, M. F., in *Report LA-12669-MS*. Los Alamos National Laboratory, Los Alamos, NM, 1994.
4. Hall, E. O., *Proc. Roy. Soc. Lond. B*, 1951, **64**(381), 747.
5. Petch, N. J., *J. Iron Steel Inst.*, 1953, **174**(1), 25.
6. Ma, Q. and Clarke, D. R., *J. Mater. Res.*, 1995, **10**, 853.
7. McElhaney, K. W., Vlassak, J. J. and Nix, W. D., *J. Mater. Res.*, 1998, **13**(5), 1300.
8. Michalske, T. A. and Houston, J. E., *Acta mater.*, 1998, **46**(2), 391.
9. Nix, W. D. and Gao, H., *J. Mech. Phys. Solids*, 1998, **46**(3), 411.
10. Begley, M. R. and Hutchinson, J. W., *J. Mech. Phys. Solids*, 1998, **46**(10), 2049.

11. Fleck, N. A., Muller, G. M., Ashby, M. F. and Hutchinson, J. W., *Acta metall.*, 1994, **42**(2), 475.
12. Fleck, N. A. and Hutchinson, J. W., *J. Mech. Phys. Solids*, 1993, **41**, 1825.
13. Fleck, N. A. and Hutchinson, J. W., in *Advances in Applied Mechanics*, Vol. 33, ed. J. W. Hutchinson and T. Y. Wu. Academic Press, New York, 1997.
14. Daw, M. S. and Baskes, M. I., *Phys. Rev. B*, 1984, **29**, 6443.
15. Taylor, P. and Dodson, B. W., in *Shock Waves in Condensed Matter*, ed. Y. M. Gupta. Plenum Publishing Co, 1986, p. 287.
16. Taylor, P. and Dodson, B. W., *Phys. Rev. B*, 1987, **36**(2), 1355.
17. Taylor, P. and Dodson, B. W., *Phys. Rev. B*, 1990, **42**(2), 1200.
18. Taylor, P., *Phys. Rev. B*, 1991, **44**(23), 13026.
19. Holian, B. L. and Lomdahl, P. S., *Science*, 1998, **280**(5372), 2085.
20. Hoagland, R. G. and Baskes, M. I., *Scripta mater.*, 1998, **39**(4-5), 417.
21. Kitamura, T., Yashiro, K. and Ohtani, R., *JSME Int. J., Ser. A*, 1997, **40**(4), 430.
22. Daw, M. S., Foiles, S. M. and Baskes, M. I., *Mater. Sci. Rep.*, 1993, **9**(7-8), 251.
23. Angelo, J. E., Moody, N. R. and Baskes, M. I., *Model. Simul. Mater. Sci. Eng.*, 1995, **3**, 289.
24. Foiles, S. M., *Phys. Rev. B*, 1985, **32**, 7685.
25. Baskes, M. I., Angelo, J. E. and Moody, N. R., in *Hydrogen Effects in Materials*, ed. A. W. Thompson and N. R. Moody. The Minerals, Metals and Materials Society, Warrendale, PA, 1996, p. 77.
26. Baskes, M. I., Sha, X., Angelo, J. E. and Moody, N. R., *Model. Simul. Mater. Sci. Eng.*, 1997, **5**, 651.
27. Horstemeyer, M. F. Baskes, M. I., Hughes, D. A. and Godfrey, A., *Int. J. Plasticity*, 2001, in press.
28. Horstemeyer, M. F. and Baskes, M. I., *J. Eng. Mater. Technol.*, 1999, **121**, 114.
29. Nose, S., *Mol. Phys.*, 1984, **50**, 255.
30. Hoover, W. G., *Phys. Rev. A*, 1985, **31**, 1695.
31. Yoshida, K., Goto, Y. and Yamamoto, M., *J. Phys. Soc. Japan*, 1966, **21**, 825.
32. Plimpton, S. J., *J. Comput. Phys.*, 1995, **117**, 1.
33. Baskes, M. I. and Daw, M. S., in *Hydrogen Effects on Material Behavior*, ed. N. R. Moody and A. W. Thompson. The Minerals, Metals and Materials Society, Warrendale, PA, 1990, p. 717.
34. Leibfried, G., *Z. Phys.*, 1950, **127**, 344.
35. Edington, J. W., *Phil. Mag*, 1969, **19**(162), 41.
36. Follansbee, P. S., in *Impact Loading and Dynamic Behavior of Materials*, ed. C. Y. Chiem, H. D. Kunze and L. W. Meyer. Informationsgesellschaft-Verlag, 1988, p. 315.
37. Horstemeyer, M. F., Lim, T. J., Lu, W. Y., Mosher, D. A., Baskes, M. I. and Prantil, V. C., Torsion/simple shear of single crystal copper, to be submitted.
38. Tabor, D., *The Hardness of Metals*. Clarendon Press, Oxford, 1951.
39. Kiely, J. D. and Houston, J. E., *Phys. Rev. B: Condens. Matter*, 1998, **57**(19), 12588.
40. Masumura, R. A., Hazzledine, P. M. and Pande, C. S., *Acta metall.*, 1998, **46**(13), 4527.
41. Kiely, J. D., Hwang, R. Q. and Houston, J. E., *Phys. Rev. Lett.*, 1998, **81**(20), 4424.